Research Article | Vol. 9, No. 3 | 1 Mar 2018 | BIOMEDICAL OPTICS EXPRESS 1232
Biomedical Optics EXPRESS

Design and implementation of a low-cost, portable OCT system

SANGHOON KIM,* MICHAEL CROSE, WILL J. ELDRIDGE, BRIAN COX, WILLIAM J. BROWN, AND ADAM WAX

Department of Biomedical Engineering, Duke University, Durham, NC 27708, USA
**Sanghoon.Kim@duke.edu*

Abstract: Optical coherence tomography (OCT) is a widely used biomedical imaging tool, primarily in ophthalmology to diagnose and stage retinal diseases. In order to increase access for a wider range of applications and in low resource settings, we developed a portable, low-cost OCT system that has comparable imaging performance to commercially available systems. Here, we present the system design and characterization and compare the system performance to other commercially available OCT systems. In addition, future cost reductions and potential additional applications of the low-cost OCT system are discussed.

OCIS codes: (170.4500) Optical coherence tomography; (330.4460) Ophthalmic optics and devices; (300.6190) Spectrometers.

References and links

1. D. Huang, E. A. Swanson, C. P. Lin, J. S. Schuman, W. G. Stinson, W. Chang, M. R. Hee, T. Flotte, K. Gregory, C. A. Puliafito, and et, "Optical coherence tomography," Science **254**(5035), 1178–1181 (1991).
2. A. M. Zysk, F. T. Nguyen, A. L. Oldenburg, D. L. Marks, and S. A. Boppart, "Optical coherence tomography: a review of clinical development from bench to bedside," J. Biomed. Opt. **12**(5), 051403 (2007).
3. M. Adhi and J. S. Duker, "Optical coherence tomography--current and future applications," Curr. Opin. Ophthalmol. **24**(3), 213–221 (2013).
4. U. Schmidt-Erfurth, S. Klimscha, S. M. Waldstein, and H. Bogunović, "A view of the current and future role of optical coherence tomography in the management of age-related macular degeneration," Eye (Lond.) **31**(1), 26–44 (2017).
5. R. L. Shelton, W. Jung, S. I. Sayegh, D. T. McCormick, J. Kim, and S. A. Boppart, "Optical coherence tomography for advanced screening in the primary care office," J. Biophotonics **7**(7), 525–533 (2014).
6. Y. S. Zhang, J. B. Chang, M. M. Alvarez, G. Trujillo-de Santiago, J. Aleman, B. Batzaya, V. Krishnadoss, A. A. Ramanujam, M. Kazemzadeh-Narbat, F. Chen, P. W. Tillberg, M. R. Dokmeci, E. S. Boyden, and A. Khademhosseini, "Hybrid Microscopy: Enabling Inexpensive High-Performance Imaging through Combined Physical and Optical Magnifications," Sci. Rep. **6**(22691), 22691 (2016).
7. J. C. Contreras-Naranjo, Q. S. Wei, and A. Ozcan, "Mobile Phone-Based Microscopy, Sensing, and Diagnostics," IEEE J. Sel. Top. Quantum Electron. **22**(3), 1–14 (2016).
8. S. Knowlton, A. Joshi, P. Syrrist, A. F. Coskun, and S. Tasoglu, "3D-printed smartphone-based point of care tool for fluorescence- and magnetophoresis-based cytometry," Lab Chip **17**(16), 2839–2851 (2017).
9. C. D. Lu, M. F. Kraus, B. Potsaid, J. J. Liu, W. Choi, V. Jayaraman, A. E. Cable, J. Hornegger, J. S. Duker, and J. G. Fujimoto, "Handheld ultrahigh speed swept source optical coherence tomography instrument using a MEMS scanning mirror," Biomed. Opt. Express **5**(1), 293–311 (2014).
10. W. Jung, J. Kim, M. Jeon, E. J. Chaney, C. N. Stewart, and S. A. Boppart, "Handheld optical coherence tomography scanner for primary care diagnostics," IEEE Trans. Biomed. Eng. **58**(3), 741–744 (2011).
11. Z. Wang, H. C. Lee, D. Vermeulen, L. Chen, T. Nielsen, S. Y. Park, A. Ghaemi, E. Swanson, C. Doerr, and J. Fujimoto, "Silicon photonic integrated circuit swept-source optical coherence tomography receiver with dual polarization, dual balanced, in-phase and quadrature detection," Biomed. Opt. Express **6**(7), 2562–2574 (2015).
12. P. Pande, R. L. Shelton, G. L. Monroy, R. M. Nolan, and S. A. Boppart, "Low-cost hand-held probe for depth-resolved low-coherence interferometry," Biomed. Opt. Express **8**(1), 338–348 (2017).
13. J. Fujimoto and E. Swanson, "The Development, Commercialization, and Impact of Optical Coherence Tomography," Invest. Ophthalmol. Vis. Sci. **57**(9), OCT1 (2016).
14. J. P. Rolland, P. Meemon, S. Murali, K. P. Thompson, and K. S. Lee, "Gabor-based fusion technique for Optical Coherence Microscopy," Opt. Express **18**(4), 3632–3642 (2010).
15. M. Wojtkowski, R. Leitgeb, A. Kowalczyk, T. Bajraszewski, and A. F. Fercher, "In vivo human retinal imaging by Fourier domain optical coherence tomography," J. Biomed. Opt. **7**(3), 457–463 (2002).
16. P. Mailankody, R. Battu, A. Khanna, A. Lenka, R. Yadav, and P. K. Pal, "Optical coherence tomography as a tool to evaluate retinal changes in Parkinson's disease," Parkinsonism Relat. Disord. **21**(10), 1164–1169 (2015).

#314842 https://doi.org/10.1364/BOE.9.001232
Journal © 2018 Received 4 Dec 2017; revised 13 Feb 2018; accepted 14 Feb 2018; published 20 Feb 2018

Biomedical Optics EXPRESS

17. V. Manjunath, J. Goren, J. G. Fujimoto, and J. S. Duker, "Analysis of choroidal thickness in age-related macular degeneration using spectral-domain optical coherence tomography," Am. J. Ophthalmol. **152**(4), 663–668 (2011).

1. Introduction

OCT is a non-invasive optical imaging technique that utilizes low coherence interferometry to detect backscattered light from tissue to produce depth resolved images up to a few millimeters below the surface [1]. OCT is an emerging technology for a wide range of biomedical applications including intravascular OCT (IV-OCT) for identifying at-risk atherosclerotic plaques, detection of neoplasia in the gastrointestinal tract and other organ systems, real-time surgical guidance, and high resolution imaging of biological specimens [2]. However, OCT has made the largest impact in the field of ophthalmology. Due to its fast speed and high sensitivity, spectral domain OCT (SD-OCT) is currently recognized as the state of the art technology for acquiring *in vivo*, cross sectional image of ocular tissues to identify retinal morphology and abnormalities [3, 4]. Although OCT has been adopted as the gold standard for retinal imaging in ophthalmology, the high cost of clinical systems (up to $150,000) has restricted access to mostly large eye centers and laboratories [5]. Thus, development towards a low-cost, portable OCT system could significantly increase the ease of access, particularly in low resource settings, and expand the use of OCT to a wider range of applications which were previously cost prohibitive.

Cost reduction and system portability have been of interest for numerous optical technologies for development as point of care medical applications. These optical imaging modalities includes fluorescence microscopy [6], computational microscopy [7] and cytometry [8]. For OCT, multiple research groups have developed various portable and small OCT systems which incorporate handheld scanners. Lu et al. demonstrated a handheld high speed swept-source OCT, and reduced the form factor by using a MEMS mirror instead of galvanometer mirrors [9]. Jung et al. developed a handheld OCT system for primary care diagnostics [10]. However, the OCT system engines of these systems (which include the light source, spectrometer, PC, and interferometer optics) are still bulky and expensive which limit application of these systems for point of care imaging. Recent efforts in developing a comprehensive low-cost OCT system include a miniaturized, low-cost, fully packaged silicon photonic integrated swept-source OCT [11] and a low-cost handheld linear OCT that could be built using only standard off-the-shelf inexpensive components [12]. However, reductions in size and cost of these systems come with a significant sacrifice of SNR and reduced imaging depth.

In this paper, we describe the design and implementation of a low-cost, portable OCT system for point of care use and demonstrate imaging capabilities that could meet the required performance for retinal imaging in clinical and laboratory studies. Toward this goal, we identified several potential approaches to significantly reduce the cost of the system. First, the OCT engine can be fully constructed using commercial off-the-shelf component level parts to eliminate the overhead from margin stacking found in existing assemblies and sub-assemblies. In addition, in designing the system, we took a system level approach to cost reduction in both the selection of individual parts and the total construction of the system that meets the targeted performance, rather than focusing on optimizing an individual part. This allowed us to maintain the desired system performance even after multiple tradeoffs were made in component performance to reduce the total cost of the system.

In SD-OCT systems, the broadband light source and the spectrometer are traditionally the most expensive elements [13]. In our low-cost design, we sought to greatly reduce the cost of these two components. For the light source, we used a non-temperature controlled, fiber coupled superluminescent diode (SLD). To overcome the imaging artifacts caused by the intensity fluctuations of an uncooled SLD, the reference background is captured periodically for baseline subtraction. A custom, robust spectrometer was designed using a tall pixel CMOS line array, which greatly reduced the system's sensitivity to misalignment and

Biomedical Optics EXPRESS

temperature fluctuations and enabled the use of a 3D printed housing. The entire system is housed in a sheet metal enclosure, approximately the size of a shoe box, which includes an integrated computer.

After developing our system, we demonstrate an axial resolution of 7 μm in air, a lateral resolution of 17.6 μm, and 2.8 mm of imaging depth. We compared the device performance to a commercial OCT system (Wasatch Photonics, Spark DRC), which costs more than five times as much, and found comparable system performance. In this paper, the design and cost reduction strategy for each component are described and the feasibility of the system is characterized by comparing the acquired images to those of a commercial OCT system.

2. Instrumentation

2.1 Spectrometer

A custom spectrometer was designed using OpticStudio (Zemax). The design uses a transmission diffraction grating in a mirror – grating – lens, loop spectrometer configuration. The incoming light is fiber-coupled into the spectrometer where it is collimated using an off-axis parabolic mirror. By using a parabolic mirror as the collimating element instead of a spherical mirror before the diffraction grating, the spherical aberration within the system was significantly reduced, resulting in a smaller spot size at the detector plane. The collimated beam is diffracted using an 1852 lines/mm transmission grating (LightSmyth, T-1850-800s). The diffracted light from the grating is then focused using two, 150 mm focal length achromatic doublets (Thorlabs, AC254-150-B) onto the sensor. The schematic of the loop spectrometer is shown in Fig. 1(a). A tall pixel array CMOS sensor was used as the detector, which contained 2048 pixels with a pixel geometry of 14 μm x 200 μm. By using a tall pixel geometry, the spectrometer is designed to be more tolerant to aberration along the tall pixel axis which is perpendicular to the spectral dimension. The spot size can be optimized along the spectral dimension while sacrificing the beam diameter along the perpendicular axis to maintain the spectral resolution and throughput (Fig. 1(b-d)). In addition, this detector geometry is more robust to system misalignment due to temperature fluctuations and mechanical stress. The predicted spot size at the detector plane was under 10 μm RMS radius at the center wavelength, which was well below the pixel size of the sensor array. The detector has a 10 MHz clock rate, which enabled approximately a 5 kHz line rate with the full array. By using only half of the detector array, the line rate can be improved to 10 kHz. In practice, A-scan line rate was limited to 8.8 kHz due to overhead in readout from the detector.

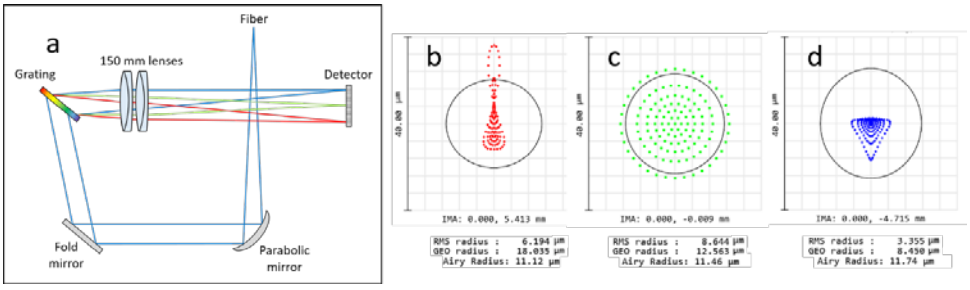

Fig. 1. (a) Schematic of the loop spectrometer. Zemax spot diagram of the loop spectrometer design (b) at 815 nm, (c) at 840 nm and (d) at 860 nm.

2.2 Light source

For the light source, a non-temperature controlled, fiber coupled superluminescent diode (3.5 mW, Exalos BTF14**)** with an 840 nm center wavelength and 45 nm full width at half maximum (FWHM) bandwidth was used. A non-temperature controlled diode source is typically avoided in designing optical imaging system due to the fluctuation of output power and spectral properties. In an interferometric system such as OCT, fluctuation in output power

Biomedical Optics EXPRESS

creates a common path artifact in the final processed OCT B-scan and also reduces image contrast. However, this issue can be fixed through regular acquisition and subtraction of the background spectrum. With the current spectrometer configuration, half of the detector array covers 62 nm bandwidth, thus acquiring data for the entire light source spectrum, but the second half of the detector can be used if a larger bandwidth source is adopted in an effort to improve axial resolution.

2.3 Scanning optics

For the scanning optics, a liquid lens design was first considered. A liquid lens is a variable focusing lens that changes its focusing power by mechanical stress or electrical control. The spherical contour of the liquid lens can be precisely controlled to adjust its focal length from a couple of centimeters to infinity. In addition, by adding more electrodes, the shape of the lens can be further controlled to enable beam steering. To determine the feasibility of using liquid lenses for OCT scanning, two liquid lenses (Varioptic, Baltic 617) were used to scan a beam, and the spot size was measured by taking the beam intensity image with a camera at the focal plane (Fig. 2(a)). While a single lens can only tilt the beam at a maximum angle of ± 0.6° with step resolution of 0.01°, using two lenses in combination doubled the angular scan range and achieved over 3 mm by 3 mm xy field of view (FOV) based on a 75 mm focal length. However, due to the smaller aperture of the liquid lens (2.4 mm in diameter), the spot size at the sample plane ranged from 40 μm on the optical axis to approximately 90 μm at the edge of the scan range, as shown in the Fig. 2(b). The large spot size at the edge of the FOV is largely due to field curvature which can be compensated by changing the focal length of the liquid lens near the edge of FOV. The optimal focusing value of the liquid lens was found by maximizing the intensity of the spot, and an approximate 30% reduction in spot size was achieved as shown in Fig. 2(c). Using this method, a spot size under 65 μm was achieved across the entire 4.4 mm diagonal scanning range, as shown in Fig. 2(b-d). The FWHM of the spot size was measured across the vertical and horizontal axis of each spot, and the average of the two measurements was reported. The liquid lens scanning system was incorporated into the low-cost OCT engine and an example OCT scan was acquired of a tape phantom on a business card, shown in Fig. 2(e). However, the dynamic focusing scheme was found to limit the speed of data acquisition; thus, the tape phantom image was acquired with a fixed focal length on the liquid lens.

Although we were able to successfully demonstrate a scanning OCT system using a liquid lens configuration, the spot size of the scanning system greatly limits its utility in biological and clinical applications where a spot size of under 20 μm is desirable for high lateral resolution. In addition, the liquid lens implementation was also limited by its response time. The liquid lens has a typical response time of 20 ms to change the focal power, and 50 ms to tilt the beam. In addition, the liquid lens exhibits hysteresis and often behaves non-linearly at high scanning rates, so only a 10 Hz scanning rate could be reliably achieved in free scanning mode. A faster scanning rate is required to provide a comfortable level of real time feedback. It is also crucial in imaging biological samples in order to limit the motion artifact across B-scans. In typical OCT systems, the acquisition speed of the detector, rather than the scanning rate, is the rate limiting step for the system. Typical frame rates for commercially available OCT systems ranges from 20 to 40 frames per second for 512 or 1024 A-scans. Thus, current liquid lens technology does not offer sufficiently high scanning rates, or a large enough aperture lens to produce a small enough spot size, constraining the application of liquid lenses for OCT beam steering.

Biomedical Optics EXPRESS

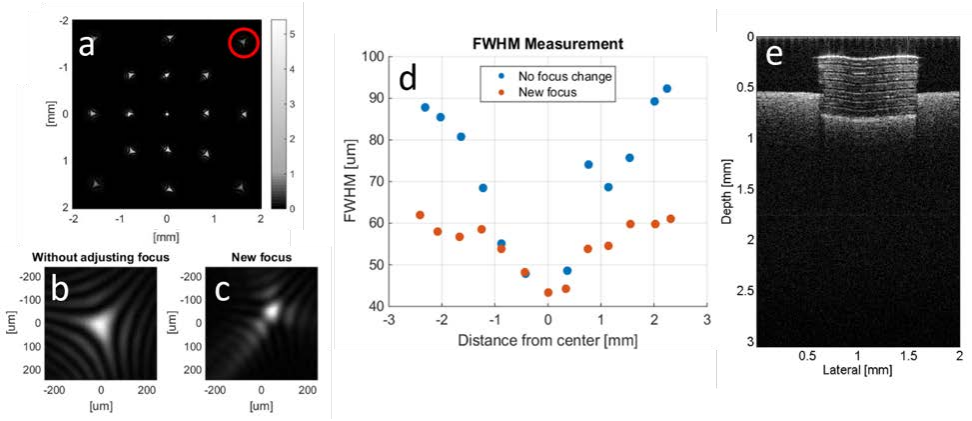

Fig. 2. (a) The measured intensity of the beam scan captured by a camera at the focal plane using two liquid lenses. (b) The spot profile without adjusting focus at the edge of the scan marked by the red circle in (a). (c) The spot profile after refocusing. (d) FWHM spot size measurements at different distance from the center without adjusting focus and with new focus. (e) An example OCT scan of a tape phantom on a business card.

To overcome this issue, an alternative scanning approach was developed using a microelectromechanical (MEMS) mirror and a liquid lens. The MEMS mirror has a larger aperture compared to the liquid lens, resulting in a smaller spot size. In addition, the overall scanning speed was increased by assigning the scanning and dynamic focusing control to two independent optical elements. With this approach, the acquisition speed of the sensor becomes the limiting step in acquisition speed. Using a 3.6 mm MEMS mirror (Mirrorcle) and 10 mm liquid lens (Optotune) a 17.6 µm FWHM spot size was obtained at the center of a 7 mm x 7 mm FOV, based on a 30 mm focal length (Fig. 3 (a)). The spot size remained under 24 µm with significantly less aberration compared to the liquid lenses scanning configuration across the entire scanned FOV. By dynamically changing the focal length of the liquid lens near the edge of the FOV, the 23.5 µm spot (red circle, Fig. 3(a)) was refocused to under 20 µm as shown in Fig. 3(b) and (c). The FWHM spot size measurement without adjusting focus for the entire scanning FOV is summarized in Fig. 3(d). It is important to note that using a liquid lens in the OCT scanner offers an additional advantage of enabling dynamic focusing at multiple depths [14]. This allows the system to adjust its focal plane to anywhere within the imaging depth FOV without manually moving the sample to the focus.

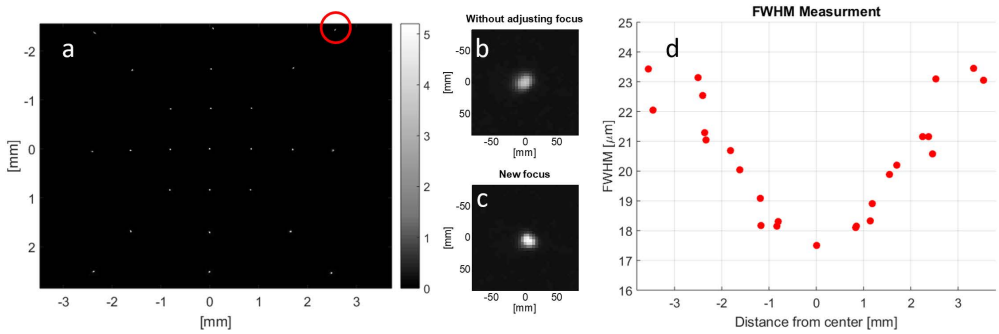

Fig. 3. (a) The measured intensity of the beam scan at the focal plane using a MEMS mirror and a liquid lens set up. (b) The spot profile without adjusting focus at the edge of the scan marked by the red circle in (a). (c) The spot profile after refocusing. (d) FWHM spot size measurements at different distance from the center without adjusting focus. Using refocusing method, a spot size under 20 µm was achieved across the entire 7 mm FOV.

Biomedical Optics EXPRESS

2.4 PC/Synchronization

A mini PC (Intel NUC5I5RYK) was integrated to further miniaturize the system. The mini PC remarkably improves the portability of the system, by eliminating the need for an external PC or laptop as is used in most commercial OCT systems. In order to synchronize the MEMS mirror to the detector array, a microcontroller (Arduino, UNO Board Rev3) was used for triggering. The Arduino was programmed to recognize the first pulse from the sensor output pulse train and send a trigger to scan the MEMS mirror without introducing a delay. The Arduino detects the time gap between pulse trains (B-scans) which cues the Arduino to again reset the scan and await the start of the subsequent pulse train. The PC controls the liquid lens and initiates the Arduino through the USB port. The Arduino enables the SLD, and manages triggering and synchronization of the spectrometer camera and the MEMS mirror. The PC reads frames from spectrometer through a USB 3.0 port and processes the received frames for display. The system schematics with control flow is summarized in Fig. 4.

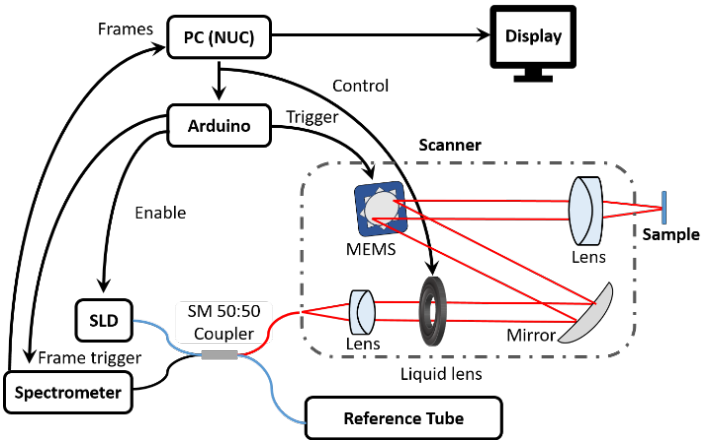

Fig. 4. The system schematic using the Arduino for synchronization.

2.5 Optical assembly

The majority of the optical assembly components, including the scanner and spectrometer housing, SLD and Arduino mounts, fiber polarization paddles, and fiber management spools, were fabricated using 3D printing technology (MakerBot Replicator 2X and Formlabs Form2) using acrylonitrile butadiene styrene (ABS) and Tough FLT0T04 materials, respectively. In addition, the 3D printed parts were designed to be more compact and lightweight compared to those found in most commercially available systems. The mini PC was mounted on the top of the OCT housing in such a way that the cooling fan of the mini PC serves as a cooling fan for the entire system (Fig. 5(a)) while also allowing easy access to the PC power switch and USB ports. Finally, the reference arm optics were mounted in adjustable lens tubes such that the path length and intensity of the reference beam can be easily tuned while conserving space and cost. The distance between lenses in the tube can be adjusted manually to defocus the beam on the mirror at the end of the reference arm. This changes the intensity of the reference beam coupled back into the optical fiber. A second adjustable lens tube allows manual adjustment of path length. An image of the system interior is shown in Fig. 5(b).

Biomedical Optics EXPRESS

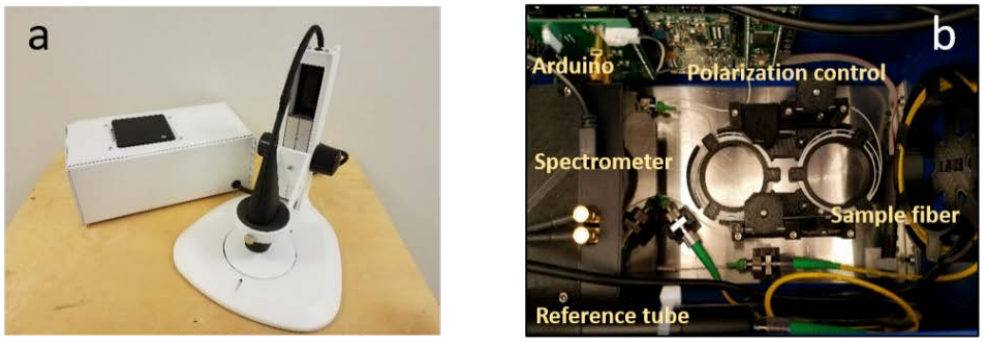

Fig. 5. (a) The low-cost system engine and (b) top view of the system interior.

2.6 Software development

In the prototyping stage, both MATLAB and LabVIEW were used to control individual subsystems within an integrated LabVIEW interface for image acquisition and processing. A custom MATLAB program was used to control the voltage driven MEMS scanning mirror. The control sequence is based on setting the controller for the MEMS mirror to await a trigger signal from the Arduino, to start pre-determined scanning by MATLAB. The camera capture sequence and real time image processing were performed with LabVIEW. For SD-OCT, typical image processing steps include background subtraction, interpolation of evenly spaced wavelength data into evenly spaced wavenumber data, dispersion compensation, and Fourier transformation [15]. The two rate determining steps for the combined software control scheme were the acquisition speed of the camera and the wavelength to wavenumber interpolation step. For B-scans consisting of 512 A-scans, 12 frames per second (fps) was achieved without the interpolation step, and 8 fps was achieved with a spline interpolation step included.

In order to improve the interpolation speed and the entire OCT processing time, GPU processing (Intel HD Graphics 6000) was implemented. With this approach, OCT processing is performed entirely on the GPU using OpenCL. This software routine is a custom Windows application written in C# and C + + . With GPU processing, a single B-scan is processed in under ten milliseconds, so that the image processing, including interpolation, no longer limits the frame rate. The B-scan rate with this approach is 12 frames per second and is limited entirely by the acquisition speed of the line scan sensor.

3. Results

The current system has an experimentally measured axial resolution of 7 μm, a lateral resolution of 17.6 μm, and an imaging depth of 2.8 mm for 7 mm x 7 mm FOV with 700 μW sample power. The detector has a B-scan acquisition rate (512x512 pixels) of 12 frames per second, and the total weight of the system including the PC and handheld scanner is 6 lbs. The total component cost for the fully functional system was under $7,200 (Table 1).

Biomedical Optics EXPRESS

Table 1. Component Cost of Low-Cost OCT systems.

Component	Price
Spectrometer	
Detector	$1,200
Lenses	$420
Grating	$245
Grating Mount	$275
Folding Mirrors	$110
Subtotal	**$2,250**
Scanner	
MEMS mirror and driver	$2,000
Liquid lens and driver	$696
Lenses and mirrors	$180
Subtotal	**$2,876**
Optical Components	
SLD and driver	$536
Optical fiber	$179
Fiber splitter	$225
Reference arm optics	$316
Subtotal	**$1,256**
Electronics	
PC and accessories (USB hub, USB and HDMI cables)	$750
Arduino and Arduino shield	$32
Subtotal	**$782**
Total	**$7,164**

To compare the performance of the low-cost OCT system to a commercially available system, an OCT scan (10 frames average) of a Scotch Giftwrap tape phantom was acquired with the low-cost system, shown in Fig. 6(a), and with a commercial Wasatch OCT system, shown in Fig. 6(b). Although the low-cost OCT system has a lower axial and lateral resolution, it has a greater imaging depth and has the capability to resolve individual tape layers throughout the entire 2.8 mm imaging depth. Note the difference in the imaging depth and FOV of the images from the two different systems.

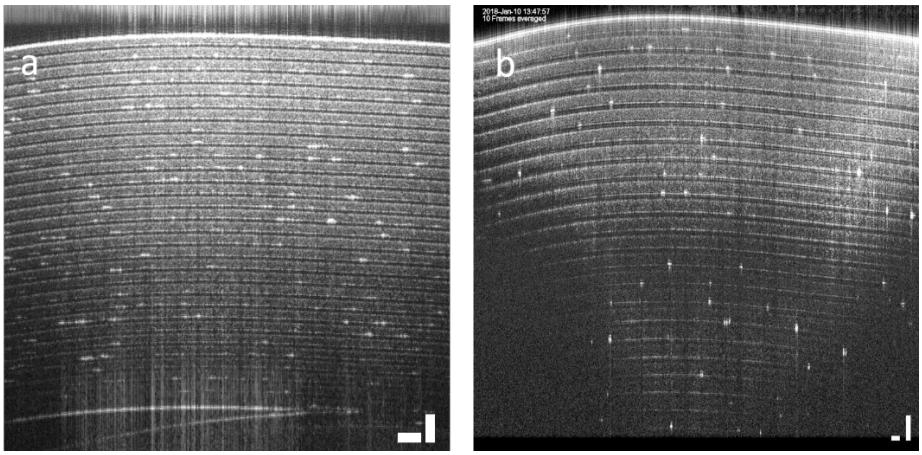

Fig. 6. OCT image of scotch tape using the (a) low-cost OCT system (scale bar, 200 μm) and (b) Wasatch commercial system (scale bar, 100 μm). The difference in scale bar comes from different imaging depth and FOV of the systems.

The system specifications of the low-cost and Wasatch OCT system, along with another entry level commercially available system (Thorlabs, Callisto CAL110C1) are summarized in Table 2. The system parameters for the low-cost system and the form factor for all systems

Biomedical Optics EXPRESS

were calculated and measured experimentally, while the system specifications and imaging performance for the commercial systems are those specified by the corresponding vendors.

Table 2. Specs of the low-cost OCT engine and commercial OCT systems.

	Low-cost OCT	Wasatch	Callisto
Price	$7,164	$45,000[a]	$35,000
System Specifications			
Center Wavelength	830 nm	830 nm	930 nm
Number of pixels per A-Scan	512	1024	512
SLD Bandwidth (3db FWHM)	45 nm	155 nm	
Maximum output power	700 µW	750 µW	
Imaging Performance			
Imaging Depth (in air)	2.8 mm	1.9 mm	1.7 mm
Axial resolution (in air)	7.0 µm	2.0 µm	7.0 µm
Lateral resolution	17.6 µm	10 µm	8 µm
A-scan rate	8.8 kHz	40 kHz	1.2 kHz
Sensitivity	99.4 dB	100 dB	107 dB
Scan range (X and Y)	7 mm	5 mm	10 mm
Form Factor			
Weight (with PC) (without PC)	6 lbs	44 lbs 19 lbs	27.6 lbs
Volume	13.7 x 7.5 x 5.1 in^3 (with PC)	16.8 x 13.2 x 5.2 in^3 (without PC)	12.6 x 5.9 x 16.55 in^3 (without PC)

[a] Price from 2013 purchase.

To demonstrate the imaging capability of the system in relevant biological tissue, *ex vivo* porcine eyes and murine skin were imaged. The low-cost OCT system can clearly resolve the tear film, epithelium, Bowman's layer, stroma, and posterior endothelium of the porcine eye as shown in Fig. 7(a). A common path artifact can be seen as a horizontal line in the image but using background subtraction, this artifact was removed in subsequent images. The lens and iris (Fig. 7(b)) and iridocorneal angle (Fig. 7(c)) of the eye were also imaged and shown below. Finally, an image of murine skin was acquired, showing epidermis, dermis and hypodermis layers. The low-cost OCT system was capable of resolving layers and structures in these biological samples.

Biomedical Optics EXPRESS

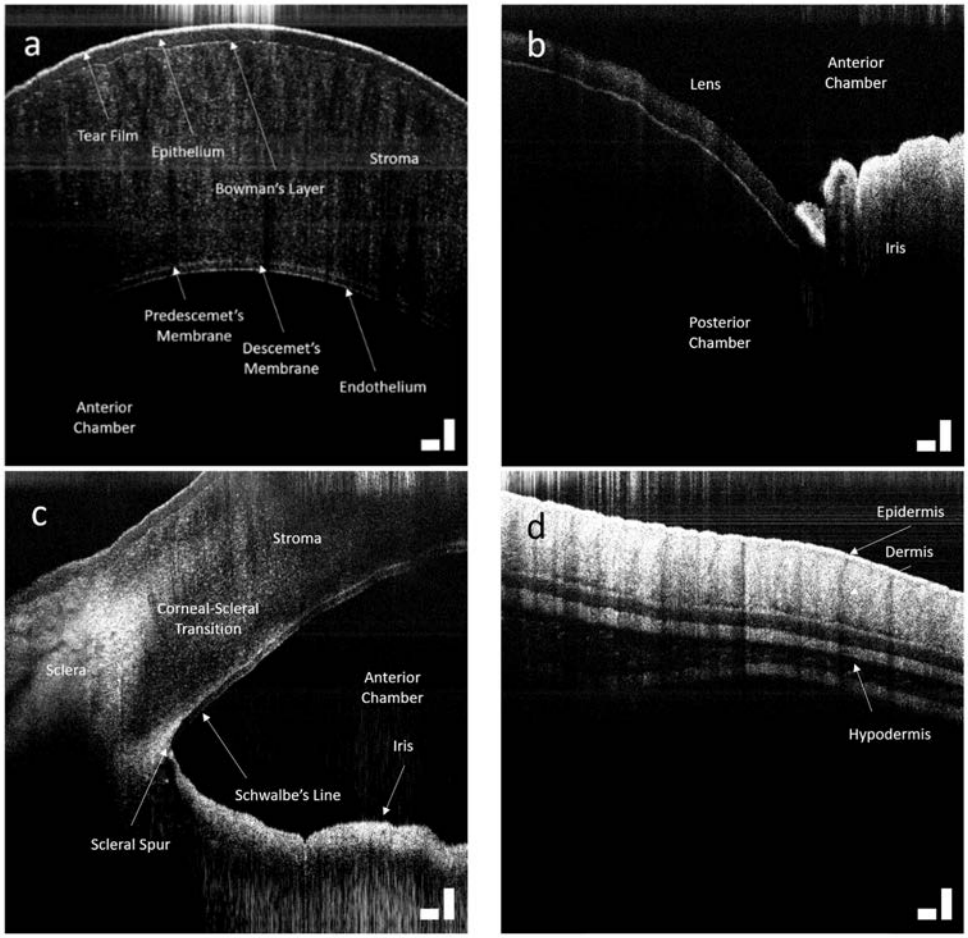

Fig. 7. OCT image of (a) a pig cornea, (b) lens and iris, (c) and iridocorneal angle. (d) OCT image of murine skin. The scale bar represents 200 μm. The images shown are 10 frame averages and the depth is given for optical path in air.

Lastly, live mice retinas were imaged. Prior to experimental imaging, a mouse retina was modeled in Zemax to determine the optimal collimating and focusing elements to in the OCT scanner to achieve a 16.4 μm diffraction limited spot on the simulated mouse retina. The 30 mm focusing lens was exchanged for a pair of 50 mm focal length achromatic lenses for a tighter spot and to enable imaging of the mice retina without any contact. The design of the scanning assembly allows easy exchange of the distal optic without opening the scanner. The mice were anesthetized prior to placement in the OCT scanner and subsequent imaging under an IACUC approved protocol. Although motion artifacts from breathing prevented B-scan averaging, a single B-scan image can clearly resolve the retinal layers [16] including retinal nerve fiber layer (RNFL), ganglion cell layer (GCL), inner plexiform layer (IPL), inner nuclear layer (INL) outer plexiform layer (OPL), outer nuclear layer (ONL), external limiting membrane (ELM), inner segment/outer segment junction (IS-OS), retinal pigment epithelium (RPE) and optical nerve head (ONH) as shown in Fig. 8. Since we did not use any eye drops or contact lens for hydration of the mouse eye while the eye were held open, the lens became opaque during imaging. The image on the right (Fig. 8(b)) shows degradation in contrast and SNR due to the dehydration of the lens.

Biomedical Optics EXPRESS

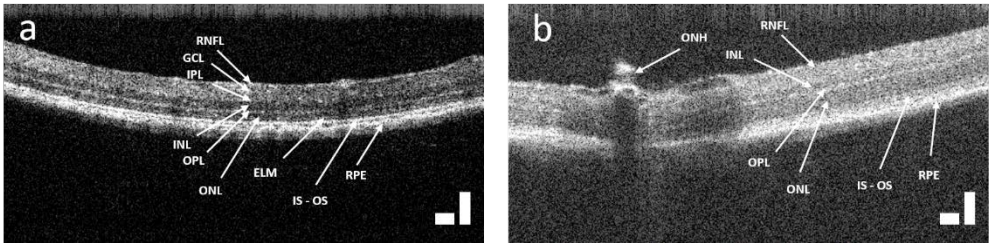

Fig. 8. (a) OCT image of a live mice retina. (b) OCT image of the same mice showing the optical neve head. The image on the right (b) has lower contrast and SNR due to the dehydration of the lens during imaging. The scale bar represents 200 μm in air.

4. Discussion

We presented a low-cost, portable OCT system with 5-fold cost reduction and more than 2-fold size reduction in volume compared to commercial OCT systems with similar imaging performance. The reported reduction in size excludes the additional volume needed for the PC for other commercial systems while the low-cost system includes the PC within the system housing. This low-cost OCT device offers an axial resolution of 7 μm in air, and a lateral resolution of 17.6 μm for 2.8 mm of imaging depth over a 7 mm FOV with 700 μW sample power. The software was developed to update 512 by 512 B-scans at 12 fps using GPU processing. During the system design, tradeoffs were made to meet the desired performance while minimizing expense. Towards this goal, we compartmentalized the system into several sub-systems (i.e. spectrometer, scanner, light source, internal optical components, and synchronization control). Rather than simply selecting the cheapest components throughout the system, each unit was intentionally designed based on the combination of components that yielded the lowest cost yet maintained the required clinical-level performance of the unit.

When designing the spectrometer, a tall pixel CMOS line scan array was used to allow the system to be more robust to misalignment and temperature fluctuations. The use of a non-temperature controlled superluminescent diode was enabled by regularly updating the background subtraction to avoid imaging artifacts. Most of the optical element mounts and mechanical components were 3D printed to fit within the system, resulting in a compact system under 6 lbs in a 14 by 7.5 by 5 inch case. The forgiving spectrometer design further opened the possibility to utilize 3D printed parts which greatly reduced the total cost of the system by manufacturing mechanical components for a fraction of the cost of machined components. For the scanning optics, a liquid lens design was first considered due to its compactness and cost. However, the liquid lens scanning geometry did not provide adequate scanning at rates higher than 10 Hz. Instead of using a liquid lens pair for beam steering, the final design utilized a MEMS scanning mirror and a single liquid lens to enable scanning with dynamic focusing at different depths of interest. Lastly, the use of an Arduino bridged all of the implemented units and acted as a master timing device for synchronizing all timing events.

In this study, we have demonstrated the capability of the system to image *ex vivo* porcine eye and murine skin as well as *in vivo* mouse retina. Clinically, OCT systems have been used for monitoring the progression of age related macular degeneration (AMD) by evaluating choroidal thickness [3]. The thickness of the choroid in healthy eyes has been reported to be 287 ± 76 μm for 54 eyes and 272 ± 76 μm for 34 eyes with the Spectralis OCT (Heidelberg Engineering) and Cirrus OCT systems (Carl Zeiss Meditec) while that of wet AMD and dry AMD was reported to be 194.6 ± 88.4 μm for 40 eyes and 213.4 ± 92.2 μm for 17 eyes respectively [17]. Thus, with the 7 μm axial resolution of the low-cost OCT system, the difference between the choroidal thickness of healthy patients and the patients with AMD could be measured accurately, if sufficient penetration depth was realized. Although the *in vivo* mice retinal image in Fig. 8 did not capture choroidal layers, we note that retinal imaging

Biomedical Optics EXPRESS

is more difficult in mice than in humans and thus deeper penetration is possible in humans. The aberration and degradation from the mouse eye contribute to worse imaging performance, and future imaging on human subjects will be performed to determine the clinical utility of the system. In addition, the images of the porcine eye show the potential to detect and measure the anterior chamber angle as well as the corneal thickness for open-angle glaucoma. These images of tissue samples demonstrate that the system performance is sufficient for detecting features that are commonly used for pathological diagnosis in ophthalmology.

The greatest limitation of the current system is its acquisition speed. The B-scan rate is limited entirely by the acquisition speed of the line scan sensor. While imaging performance of a single frame is comparable to faster systems, the system cannot take advantage of the potential SNR improvement obtained through averaging. When live mice were imaged with the system, breathing motion caused motion artifact to appear when multiple B-scan images were averaged. However, the sensor offers clear advantages; it is inexpensive and permits the spectrometer geometry to remain aligned in the presence of temperature and mechanical perturbations. Further, the bit depth of the sensor is higher than many other available line scan sensors in the same price range. We are currently considering alternative sensors to improve acquisition speed, however further price reduction is our primary goal for the next generation system.

In the future, further optimization and customization will be pursued to reduce the total cost of the system while also increasing functionality and portability. There has been great interest in miniaturizing OCT systems targeted for primary care medicine, and many handheld laboratory-based and commercial OCT systems have been developed for *in vivo* human retinal imaging. However, the optical engines of these systems have remained bulky which has limited the point of care application of OCT diagnostics. Our device weighs less than 6 lbs including the PC and the handheld scanner, but the form factor can be further reduced by developing customized control electronics and integrating battery power. For example, the controller boards for the MEMS mirror and liquid lens can be custom designed using a much simpler electronic circuit board, which will both contribute to further cost reduction of the system and reduce system size. The system currently consumes only 14 Watts when fully functioning, so it is feasible to replace the PC with a system on a module (SOM) and convert to a fully battery powered system. Future imaging work will be performed to evaluate the diagnostic performance of the low-cost OCT system for *in vivo* human retinal imaging.

5. Conclusion

We have developed a low-cost OCT system which cost $7,200 for the components which include a PC, light source, customized spectrometer, and 3D printed mechanical parts. The performance of the system has been characterized by measuring optical parameters such as the power throughput, and lateral resolution. These compared favorably to currently available commercial OCT systems. The capability of the system was demonstrated by imaging an *ex vivo* porcine eye and an *in vivo* mouse retina, as well as murine skin. Future work on the system will aim to further optimize the frame rate of the system to match commercially available systems and to further improve the portability of the system for point of care clinical imaging.

Funding

National Science Foundation (NSF) (EAGER1445992); National Institute of Health (NIH) (R01 CA210544); Duke-Coulter Translational Partnership

Disclosures

AW, MC: Lumedica, Inc. (I,C), WJB: Lumedica, Inc. (I,E), BC: Lumedica, Inc. (C)